




Design and development of a multiwalled carbon nanotubes-based copper (II) Schiff base complex for the facile non-enzymatic electrochemical sensing of glucose

Rashmi Gupta¹, Mamta Yadav¹, Smita Singh¹, Vellaichamy Ganesan¹, and Bachcha Singh^{1,*} 

¹Department of Chemistry, Centre of Advance Study, Institute of Science, Banaras Hindu University, Varanasi 221005, India

Received: 5 March 2023

Accepted: 11 July 2023

Published online:

2 August 2023

© The Author(s), under exclusive licence to Springer Science+Business Media, LLC, part of Springer Nature 2023

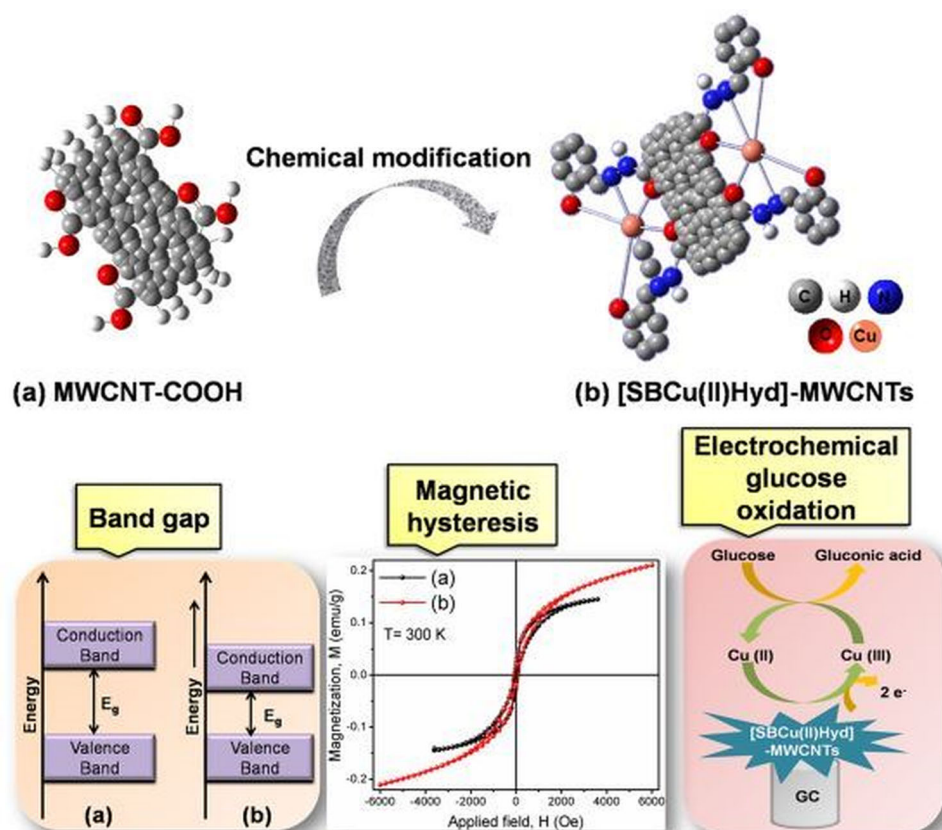
ABSTRACT

A new bifunctional nanomaterial, [SBCu(II)Hyd]-MWCNTs, exhibiting exotic electrical and magnetic properties has been synthesized via chemical modification of MWCNT-COOH. Double probe DC electrical conductivity, CV and EIS studies show better conductivity of the material than that of MWCNT-COOH. With higher saturation and remanent magnetization, as well as coercivity, [SBCu(II)Hyd]-MWCNTs showed better ferromagnetic characteristics. Mott-Schottky electrochemical analysis was carried out to explore capacitive and dielectric properties. The enhancement in electrical conductivity of [SBCu(II)Hyd]-MWCNTs is also confirmed by optical and electrochemical band gaps studies. Subsequently, this material has been utilized to fabricate an electrochemical sensor by coating it over glassy carbon electrode for the determination of glucose. The corresponding sensitivity and limit of detection values are calculated to be $1.1 \mu\text{A } \mu\text{M}^{-1} \text{ cm}^{-2}$ and $0.09 \mu\text{M}$, respectively.

Handling Editor: Annela M. Seddon.

Address correspondence to E-mail: bsinghbhu@rediffmail.com

GRAPHICAL ABSTRACT



Introduction

The design, fabrication and processing of nanoscale materials having targeted properties and functions are absolutely exciting challenges. Functional nanomaterials are the backbone of newly emerging nanotechnologies. Due to intrinsic quantum size, shape, unique chemical and physical properties, these materials have great potential for various applications including electronics, bioelectronics, optoelectronics [1], electrochemical sensors [2], therapeutics [3], energy conversion & storage devices [4], catalysis [5] and many other domains [6]. Schiff bases and their metal complexes have recently piqued the interest of coordination chemists because of their potential applications in plethora of domains, such as catalysis [7, 8], biology [9, 10], electrochemical

sensing [11–13], cancer treatment [14, 15], energy storage, and magnetic and electronic devices [16–20]. Due to ease of synthesis, availability, stability, structural variability, versatile coordinating capabilities, electronic and magnetic properties, Schiff bases are often referred to as “Privileged Ligands” [12]. The hydrazones, Schiff base of hydrazides, exhibit fascinating ligational properties. These have several chelating sites that can coordinate with transition metals in enol or keto tautomeric form [21]. Copper complexes are a significant class of molecules having many perspectives including bioinorganic, catalysis, and magnetism, etc. [22]. Copper complexes of Schiff bases have attracted a lot of interest in spin-based electronic device applications due to their diverse coordination geometries and magnetic exchange properties [23]. Moreover, these complexes have wide range of applicability in analytical chemistry

[24]. Diabetes is a chronic, metabolic disorder and occurs when the concentration of glucose is extremely high in the blood [25]. It becomes prime important to control and normalize the sugar level in diabetic patients to avoid the long-term adverse effects [26–30]. A number of techniques are in use for determination of glucose such as electrochemical, fluorescence, chromatography, colorimetric and chemi-luminescence [26, 30]. Electrochemical methods have been considered very important for the determination of glucose, because this method is simple, selective, provides quick response, good stability, cost effective as well as has low detection limit [30].

The existence of Schiff base transition metal compounds in various oxidation states has expanded their applications in the field of electrochemistry [31]. The structural and electronic properties of these complexes are responsible for interactions with the analytes and thereby improving sensor sensitivity and selectivity [11]. Carbon nanotubes (CNTs)-based electrochemical sensing platforms (ESPs) have recently been investigated for biomolecular sensing owing to their good mechanical strength, high surface area, superior electrical conductivity as well as unique thermal and chemical stability. Increase in electron transfer activity at MWCNTs electrodes facilitated oxidation of glucose and alcohol [32, 33]. Several CNTs supported transition metal nanoparticles [32, 33] and Schiff base complexes [34, 35] are documented in the literature for low potential detection of anion and non-enzymatic electrochemical glucose determination. Transition metals (i.e., copper and nickel) and their oxides are widely used for glucose measurement because these are cheap and have high catalytic efficiency [36]. Several copper and copper oxide nanoparticles-based glucose sensors are known [27, 28, 32, 36–40]. However, no research work focusing on copper Schiff base complex functionalized MWCNTs-based non-enzymatic electrochemical glucose sensors has been published to date.

In present work, synthesis of a promising electrical conducting and magnetic functional nanomaterial ([SBCu(II)Hyd]-MWCNTs) is reported. The ester functionalized MWCNTs (Est-MWCNTs) was obtained by esterification of MWCNT-COOH. This reacted with hydrazine hydrate to yield hydrazide functionalized MWCNTs (Hyd-MWCNTs), which on reaction with 2-hydroxybenzaldehyde gave

hydrazone (Schiff base) functionalized MWCNTs, i.e., SBHyd-MWCNTs. The binding of copper (II) to hydrazone moieties has led to the generation of copper centers onto the surface of MWCNTs. Several spectral (FT-IR, UV-visible, XPS and Raman), TGA, structural (PXRD, TEM and EDAX) techniques have been used to characterize the functional nanomaterials. DC electrical conductivity, electrochemical (CV and EIS) and magnetic properties of materials have been investigated. [SBCu(II)Hyd]-MWCNTs was then coated over glassy carbon electrode to form GC[SBCu(II)Hyd]-MWCNTs which was used for electrochemical sensing of glucose.

Experimental details

Materials

Carboxylic acid group functionalized multiwalled carbon nanotubes, > 8% with average diameter of MWCNTs 9.5 nm & length of 1.5 μm , hydrazine monohydrate, 2-hydroxybenzaldehyde, copper (II) acetate monohydrate, ferrocene and tetrabutylammonium perchlorate were supplied from Sigma-Aldrich Chemicals, India. High-grade organic solvents and triethylamine were received from SD fine chemicals, India. Potassium ferrocyanide, potassium ferricyanide and potassium chloride were obtained from Qualigens Mumbai, India. Silver conductive paste was purchased from Merck, India. Glucose was procured from SRL chemicals, India, and potassium hydroxide was received from Rankem, India. Sodium chloride (NaCl) and calcium chloride (CaCl_2) were procured from Merck. Acetaminophen and acetylsalicylic acid were purchased from Sigma-Aldrich. Cysteine and magnesium chloride (MgCl_2) were purchased from SD Fine chemicals. Urea and uric acid were procured from Qualigens and SRL, respectively. All chemicals and reagents were used as procured without any purification.

Instrumental techniques

In order to confirm the successful surface functionalization of MWCNTs, spectral data were acquired by FT-IR spectroscopy (PerkinElmer spectrophotometer using KBr pellets), UV-vis absorption spectroscopy (UV 1700 Pharma Spec, Shimadzu spectrophotometer in solid and solution), X-ray photoelectron

spectroscopy (AMICUS (UK) spectrometer) and XPSPEAK41 software was used for profile fitting of high-resolution XPS spectra. Raman spectra were obtained by Renishaw micro-Raman spectrometer. The measurement was performed by using a solid-state diode laser (532 nm with 0.5% intensity at 100 mW laser power). Thermogravimetric analytical data were obtained from PerkinElmer-STA 6000 instrument under N₂ atmosphere. Weight loss was recorded within the temperature range of 30 to 900 °C at a heating and flow rate of 10 °C min⁻¹ and 20.0 mL min⁻¹, respectively. Powder X-ray diffraction (PXRD) characterization was carried out using RD Bruker D8 Advance X-ray diffractometer with Cu-K α radiation ($\lambda = 0.1541$ nm). Transmission electron microscopy (TEM) images were taken on a TECNAI 20 G² microscope which is equipped with EDAX spectrometer with an acceleration voltage range of 30–200 kV. Dual probe conductivity cells were constructed in the laboratory to measure the DC electrical conductivity of materials at ambient temperature with the help of Keithley 2635B equipment. A Micro Sense LLC/ EZ9 vibrating sample magnetometer (VSM) was used to measure the field-dependent magnetization and a Quantum Design's MPMS-3 SQUID magnetometer was used to measure the temperature-dependent field cooled (FC) and zero field cooled (ZFC) magnetization. Electrochemical experiments were conducted by CHI-660 C series electrochemical analyzer (USA) employing three electrodes system; working electrode: glassy carbon (GC, area = 0.07 cm²), counter electrode: Pt wire and reference electrode: Hg/Hg₂Cl₂/KCl (saturated) and Ag/AgCl were used for aqueous & for non-aqueous solutions, respectively. The experimental electrochemical impedance spectroscopy (EIS) data were modeled with simulating software (ZsimpWin 3.21) to provide best-fitting versatile Nyquist circuit models.

Preparation of SBHyd-MWCNTs

The hydrazide functionalized MWCNTs (Hyd-MWCNTs) was prepared by using reported method [41]. MWCNT-COOH on esterification yielded ester functionalized MWCNTs (Est-MWCNTs). Hyd-MWCNTs was obtained by reaction of Est-MWCNTs with hydrazine hydrate. The synthesis of SBHyd-MWCNTs was carried out by preparing a suspension of Hyd-MWCNTs (0.2 g) in dry methanol (100 mL),

followed by the dropping addition of 2-hydroxybenzaldehyde (5 mL) to it with vigorous stirring. The reaction flask was then placed on oil bath at 64 °C and being constantly stirred for 72 h. The end product was thoroughly washed with methanol via centrifugation (at 12,000 rpm for 30–35 min). The product was vacuum dried over anhydrous CaCl₂.

Preparation of [SBCu(II)Hyd]-MWCNTs

Triethylamine (3 mL) was gradually added to a stirred suspension of SBHyd-MWCNTs (0.15 g) in dry methanol (60 mL). The reaction mixture was allowed to sonicate for 15 min. To the suspension, solution of copper (II) acetate monohydrate, Cu(OAc)₂·H₂O (1.2 g) in dry methanol (10 mL) was added drop by drop while stirring continuously. Well-dispersed reaction mixture was then subjected to reflux (at 64 °C for 72 h) and stirred vigorously. The end product was thoroughly washed with methanol and water via centrifugation (at 12,000 rpm for 30–35 min) at late as green color of decant supernatant (due to unreacted copper (II) acetate) disappears. The product ([SBCu(II)Hyd]-MWCNTs) was dried under vacuum. The protocol for synthesis of nanomaterial is provided in Fig. 1.

Electrode modification for electrochemical analysis

The GC electrodes were thoroughly polished with alumina powder (0.5 micron) using a Buehler-felt pad, then rinsed, sonicated for 10 min with triple distilled water and kept for air dry. Subsequently, 10 μ L of 0.1 wt% suspension of materials (MWCNT-COOH and [SBCu(II)Hyd]-MWCNTs) suspended in anhydrous DMF was drop casted on the top shiny surface of GC electrode. Modified electrodes have undergone CV and EIS studies after drying.

Results and discussion

The FT-IR spectra of MWCNT-COOH, Est-MWCNTs, Hyd-MWCNTs, SBHyd-MWCNTs and [SBCu(II)Hyd]-MWCNTs are given in Fig. 2 and related spectral band allocations are listed in Table 1. A significant absorption band at 3424 cm⁻¹ in the spectrum of MWCNT-COOH is attributed to the $\nu(\text{OH})$ vibration of the carboxylic (-COOH) groups of

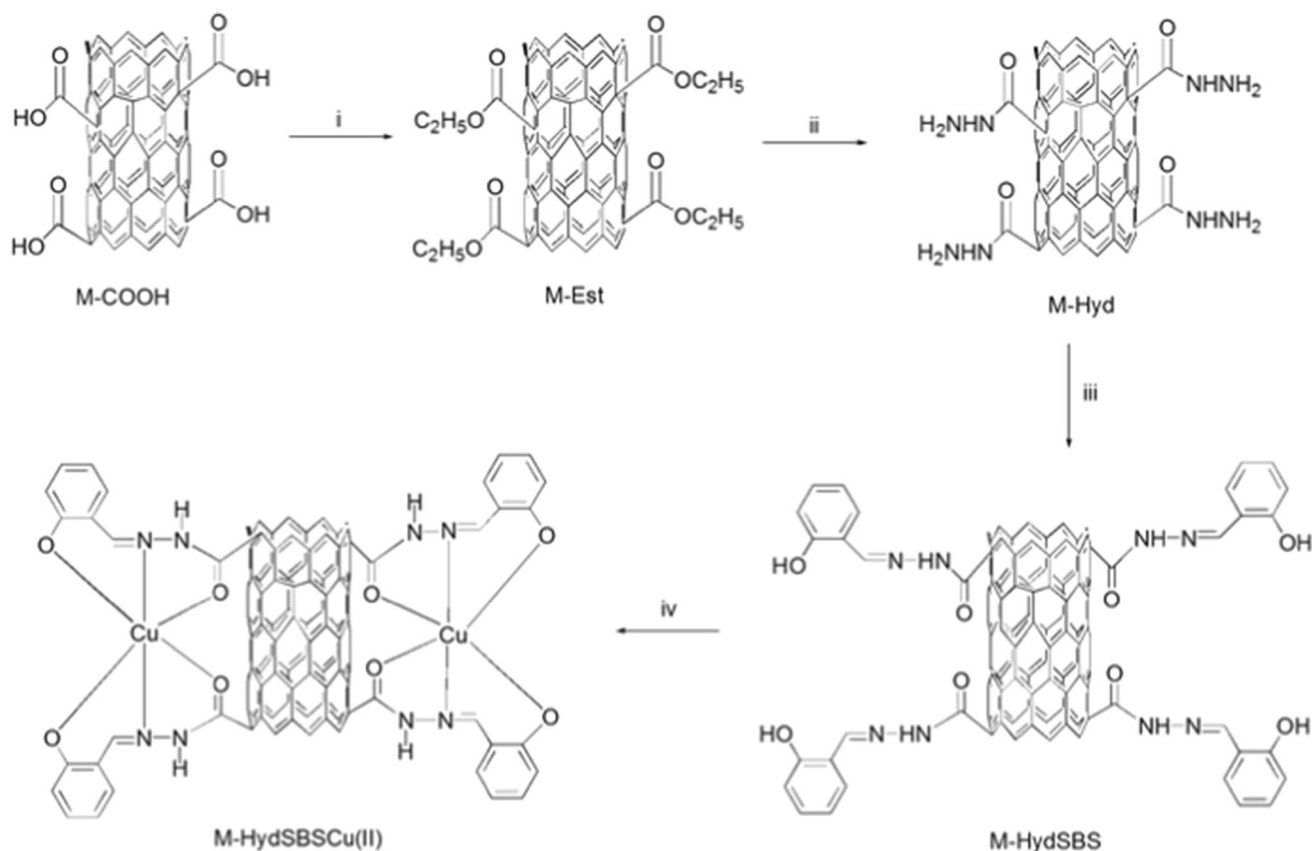


Figure 1 i EtOH (dry), conc. H₂SO₄, ii EtOH (dry), NH₂NH₂·H₂O, iii MeOH (dry), 2-hydroxybenzaldehyde, iv NEt₃, Cu(OAc)₂·H₂O.

MWCNTs [42]. The $\nu(\text{OH})$ band almost vanished in Est-MWCNTs, indicating successful esterification of MWCNT-COOH. In Hyd-MWCNTs, a strong absorption band at $\sim 3446 \text{ cm}^{-1}$ is corresponding to $\nu(\text{NH})$ of hydrazide moiety [43]. SBHyd-MWCNTs exhibited a broad absorption band at $\sim 3450 \text{ cm}^{-1}$ associated with $\nu(\text{NH})$ of hydrazone group and at 3600 cm^{-1} due to phenolic $\nu(\text{OH})$ [44]. On copper (II) incorporation, $\nu(\text{OH})$ disappeared and $\nu(\text{NH})$ band shifted to lower wave number around 3436 cm^{-1} and revealed bonding of copper (II) to azomethine nitrogen and phenoxy oxygen in [SBCu(II)Hyd]-MWCNTs [45]. The bands observed at 1743, 1755, 1641, 1648 and 1636 cm^{-1} in the FT-IR spectra of MWCNT-COOH, Est-MWCNTs, Hyd-MWCNTs, SBHyd-MWCNTs and [SBCu(II)Hyd]-MWCNTs, respectively, are assigned to the $\nu(\text{C}=\text{O})$ of the carbonyl stretching vibrations of the respective moieties. The bands due to $\nu(\text{C}=\text{N})$ of SBHyd-MWCNTs merged with $\nu(\text{C}=\text{O})$ of the carbonyl group. The absorption bands responded to the $\nu(\text{C}=\text{N})$ and $\nu(\text{C}=\text{O})$ are obtained at lower wave number in [SBCu(II)Hyd]-MWCNTs (1636 cm^{-1}) to that of

SBHyd-MWCNTs (1648 cm^{-1}). This is indicative of bonding of the $> \text{C}=\text{N}$ (azomethine nitrogen) and $> \text{C}=\text{O}$ (carbonyl oxygen) of the hydrazone with Cu (II) [45, 46]. Owing to Cu–O and Cu–N stretching vibrations, [SBCu(II)Hyd]-MWCNTs exhibit two additional vibronic bands at 522 and 427 cm^{-1} , respectively. This revealed bonding of $> \text{C}=\text{O}$ and $> \text{C}=\text{N}$ group of SBHyd-MWCNTs to copper (II) [46].

Fig. S1a shows the UV–visible absorption spectra of SBHyd-MWCNTs and [SBCu(II)Hyd]-MWCNTs in MeOH. The $\pi \rightarrow \pi^*$ transition due to sp^2 - hybridized carbon atoms of MWCNTs got merged in spectra of both the materials and appeared as a single broad peak around 240–270 nm. One more weak absorption band emerged at around 638 nm in [SBCu(II)Hyd]-MWCNTs is associated with ${}^1\text{B}_{1g} \leftarrow {}^1\text{B}_{2g}$ transition of Cu(II). This is characteristic of a five-coordinate square pyramidal geometry around copper (II). The spectra of MWCNT-COOH, SBHyd-MWCNTs and [SBCu(II)Hyd]-MWCNTs in MeOH, DMF and solid state (Nujol mull) are shown in Fig. S1 b, c & d. The onset of absorption peaks is found to shift toward

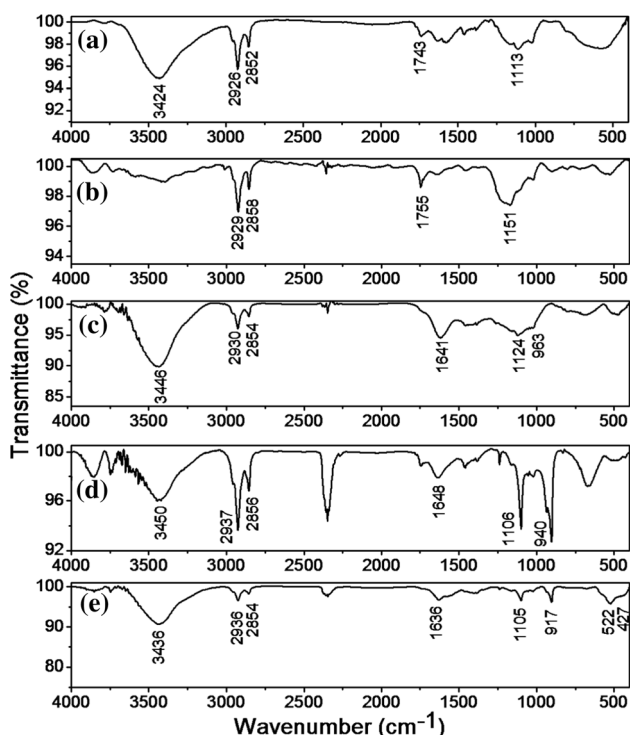


Figure 2 FT-IR spectra of (a) MWCNT-COOH, (b) Est-MWCNTs, (c) Hyd-MWCNTs, (d) SBHyd-MWCNTs and (e) [SBCu(II)Hyd]-MWCNTs.

higher wavelength in DMF compared to MeOH because of less polarity and more Lewis basicity of DMF [47]. In addition, due to increase in intramolecular interaction and aggregation within the molecules in solid state, red shift is observed in absorption bands in solid-state spectra compared to that in DMF [48].

XPS data were used to characterize the surface elemental composition, chemical state, bonding & interactions of the materials [49]. All binding energies were calibrated with reference low binding energy (284.6 eV) component of the C 1s spectrum to compensate the sample charging [50]. The wide XPS spectra of SBHyd-MWCNTs & [SBCu(II)Hyd]-MWCNTs are shown in Fig. S2a. The binding energies near 284 eV for C1s, 400 eV for N 1 s and 531 eV

for O 1 s are clearly visible in both spectra [41, 51]. The spectrum of [SBCu(II)Hyd]-MWCNTs shows photoelectron peaks of Cu 2s, Cu 2p_{3/2}, Cu 2p_{1/2}, Cu 3s, Cu 3p_{3/2}, Auger Cu near 1101, 933.8, 953.8, 121.5, 76.2 and 568–715 eV, respectively. This revealed the presence of copper in addition to C, N and O. High-resolution spectra of Cu 2p (Fig. S2b) show characteristic main peak at 933.8 eV and two satellite peaks at 941.3 and 942.0 eV for Cu 2p_{3/2} and another characteristic main peak and satellite peak appeared at 953.8 and 962.2 eV, respectively, for Cu 2p_{1/2}, which confirmed that copper metal is present in + 2 oxidation state in [SBCu(II)Hyd]-MWCNTs [52, 53]. High resolution and deconvoluted spectra of C1s, N 1s and O 1s for SBHyd-MWCNTs & [SBCu(II)Hyd]-MWCNTs are provided in Fig. S3. The measured binding energy of peaks and assignments are listed in Table 2. The appearance of two new peaks at 398.6 and 530.3 eV in the deconvoluted spectrum of N 1s (Fig. S3d) and O 1s (Fig. S3f), respectively, also suggested bonding of nitrogen and oxygen of the hydrazone moieties to the Cu (II) ions in [SBCu(II)Hyd]-MWCNTs [54].

The Raman spectra of MWCNT-COOH, SBHyd-MWCNTs and [SBCu(II)Hyd]-MWCNTs (Fig. S4) showed a characteristic band in D band region(1300–1400 cm⁻¹) due to disordered sp³ hybridized carbon atoms, while a G band appeared in the region 1500–1600 cm⁻¹ attributed to tangential vibrations of sp² hybridized carbon atoms. A broad band appeared due to the overtone of the D band at around 2680 cm⁻¹ is known as the G'' or 2D band [54]. The D, G and G'' bands originated at 1341, 1576, and 2645 cm⁻¹, respectively, in the spectrum of MWCNT-COOH. These bands were observed at higher wave numbers in the spectrum of SBHyd-MWCNTs, appearing at 1346, 1582, and 2658 cm⁻¹, respectively. Further shifting of D, G, and G'' bands was observed at higher wave numbers in in [SBCu(II)Hyd]-MWCNTs and appeared at 1351, 1589, and 2664 cm⁻¹, respectively. This may be due to

Table 1 Assignments of significant FT-IR bands (cm⁻¹) for (a) MWCNT-COOH, (b) Est-MWCNTs (c) Hyd-MWCNTs, (d) SBHyd-MWCNTs and (e) [SBCu(II)Hyd]-MWCNTs

Materials	ν_{OH} / ν_{NH}	ν_{CH}	$\nu_{C=O} / \nu_{C=N}$	$\nu_{C=C}$	ν_{C-O}	ν_{Cu-O}	ν_{Cu-N}
(a)	3424	2852, 2926	1743	1462	1113	–	–
(b)	–	2858, 2929	1755	1460	1151	–	–
(c)	3446	2854, 2930	1641	1461	1124	–	–
(d)	3450	2856, 2937	1648	1457	1106	–	–
(e)	3436	2854, 2936	1636	1423	1105	522	427

Table 2 Binding energy and peak assignments for high-resolution XPS spectra of SBHyd-MWCNTs & [SBCu(II)Hyd]-MWCNTs

Components	Assignments	Binding energy (eV)	
		SBHyd-MWCNTs	[SBCu(II)Hyd]-MWCNTs
C 1s	C–C	284.8	285.1
	C=C	284.6	284.6
	C=O	289.0	288.5
	C–N	285.8	285.8
	C=N	286.4	286.8
	C–O	286.5	286.2
N 1s	N–N	399.8	399.9
	N–H	401	400.3
	N–C	400.4	400.5
	N=C	400.2	400.9
	N–Cu	–	398.9
O 1s	C=O	532.7	533
	O–H	531.8	531.9
	O–Cu	–	530.3
Cu 2p	Cu 2p _{3/2}	–	933.8
	Satellite peak 1	–	941.3
	Satellite peak 2	–	942.0
	Cu 2p _{1/2}	–	953.8
	Satellite peak	–	962.8

increased dispersibility of MWCNTs after chemical modification [41, 55]. There is also evidence of an elevation in band intensity from MWCNT-COOH to SBHyd-MWCNTs and [SBCu(II)Hyd]-MWCNTs. The intensity ratio (I_D/I_G) has been evaluated for MWCNT-COOH, SBHyd-MWCNTs and [SBCu(II)Hyd]-MWCNTs and values were found to be 1.20, 1.27 and 1.31, respectively. The higher I_D/I_G ratio for [SBCu(II)Hyd]-MWCNTs is an indication of increased defect sites in MWCNTs on chemical modification [56].

Thermogravimetric study

Thermograms of MWCNT-COOH, Est-MWCNTs, Hyd-MWCNTs, SBHyd-MWCNTs and [SBCu(II)Hyd]-MWCNTs recorded in the temperature region 30–700 °C are shown in Fig. S5. Thermogram of MWCNT-COOH showed initially a weight loss of 6.2% due to removal of moisture in the temperature range 30–122 °C [43]. The decrease in weight by 23.1% in the temperature range 373–656 °C corresponds to removal of –COOH from MWCNT-COOH [57]. Further, a decrease in weight by 21.8% at 656–700 °C is due to decomposition of amorphous carbon and carbon nanotubes walls [43]. TGA thermogram of Est-MWCNTs suggested a weight loss of

19.4% within range 30–500 °C associated with the loss of moisture as well as decomposition of ester functional groups of MWCNTs. Furthermore, decomposition of carbon nanotube tubular structure occurred at 547–700 °C. Hyd-MWCNTs revealed the weight loss of 17.3% ranging from 30 to 573 °C attributed to the moisture loss and hydrazide functional group grafted to MWCNTs. Consequently, carbon nanotubes walls and structure begin to decompose in the temperature range 547–700 °C. Total three stages of weight loss were seen for SBHyd-MWCNTs. First stage showed the weight loss of 0.3% in the range 30–144 °C due to loss of humidity. In second stage weight loss of 8.1% is observed in the temperature range 145–551 °C; suggested removal of hydrazone moiety and weight loss of 13.6% occurred in third stage in the range 552–800 °C due to decomposition of remaining organic moieties and carbon nanotubes structure. Thermogram of [SBCu(II)Hyd]-MWCNTs revealed a total decrease in weight by 41.1% in the temperature range 30–700 °C. The first weight loss of 2.6% occurred at 30–110 °C due to removal of solvent/moisture from the complex. In second stage, weight loss of 26.4% in the temperature region 260–480 °C and a weight loss of 12.1% in third stage occurred at

540–700 °C due to decomposition of MWCNTs tubular structure.

Structural analysis

The powder diffraction patterns of MWCNT-COOH, SBHyd-MWCNTs and [SBCu(II)Hyd]-MWCNTs are shown in Fig. S6. The characteristic diffraction peaks emerging at ~ 25.3 , 42.8 and 53.5° in recorded PXRD patterns responded to (0 0 2), (1 0 0) and (0 0 4) planes of sp^2 hybridized structure of MWCNTs. This observation is commensurate with the fact that crystalline and tubular structure of the MWCNTs was not altered after chemical modification [43]. Moreover, appearance of two new less intense peaks in the diffraction pattern of [SBCu(II)Hyd]-MWCNTs at 43.1° and 50.3° corresponds to (1 1 1) and (2 0 0) planes of copper metal [58, 59] and is a clear indication of bonding of Cu (II) to SBHyd-MWCNTs.

The TEM imaging of MWCNT-COOH, SBHyd-MWCNTs and [SBCu(II)Hyd]-MWCNTs is shown in Fig. 3. The images reveal structural changes after chemical modification of MWCNTs. However, tubular structure and length of CNTs remained unaltered after chemical modification (Fig. 3 a, b and c). The average external diameters of MWCNT-COOH and SBHyd-MWCNTs are found to be 13 and 34 nm, respectively. The appearance of black spots around/ in between the CNTs walls in TEM image of [SBCu(II)Hyd]-MWCNTs confirmed that SBHyd-MWCNTs are successfully decorated with copper (II) atoms [60].

Energy-dispersive X-ray spectroscopy (EDAX) was employed to examine the surface elemental composition of MWCNT-COOH, SBHyd-MWCNTs, and [SBCu(II)Hyd]-MWCNTs (Fig. S7a, b, & c). The

weight and atomic percentage of the elemental carbon and oxygen in MWCNT-COOH, as well as the elemental nitrogen in addition to carbon and oxygen in SBHyd-MWCNTs, are significantly quantified. Moreover, the EDAX spectrum of [SBCu(II)Hyd]-MWCNTs revealed the presence of elemental copper together with elemental carbon, oxygen and nitrogen, which is the signature of successful chemical modification of MWCNT-COOH.

Magnetic studies

VSM and SQUID were used to study field and temperature-dependent magnetizations of MWCNT-COOH and [SBCu(II)Hyd]-MWCNTs. Magnetization (M) versus field (H) plots in the range -6000 to $+6000$ Oe at room temperature (300 K) are shown in Fig. 4. The ferromagnetic hysteresis exhibited by MWCNT-COOH is attributed to the presence of residual metal catalysts (Fe, Ni & Co) introduced during preparation of MWCNTs by CCVD method [61]. MWCNT-COOH exhibits coercivity (H_c , 59.94 Oe), remanent magnetization (M_r , 0.0189) and saturation magnetization (M_s , 0.144 emu/g) (Table 3). Moreover, the non-saturated open hysteresis loop for [SBCu(II)Hyd]-MWCNTs signified the super paramagnetic contribution of Cu(II) along with the ferromagnetic interaction of domains at room temperature [62]. [SBCu(II)Hyd]-MWCNTs show H_c , M_r and M_s values of 88.43Oe, 0.0196 and 0.209 emu/g, respectively. The higher H_c , M_r and M_s values of [SBCu(II)Hyd]-MWCNTs in comparison with that of MWCNT-COOH signified generation of large number of Cu (II) centers at the surface of MWCNT-COOH. The temperature-dependent magnetization for MWCNT-COOH and [SBCu(II)Hyd]-MWCNTs

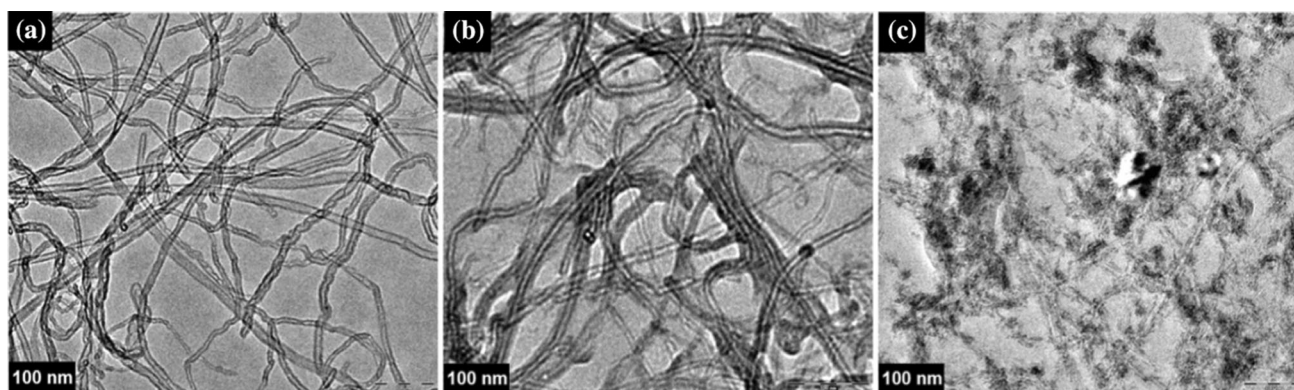


Figure 3 TEM images of (a) MWCNT-COOH, (b) SBHyd-MWCNTs and (c) [SBCu(II)Hyd]-MWCNTs.

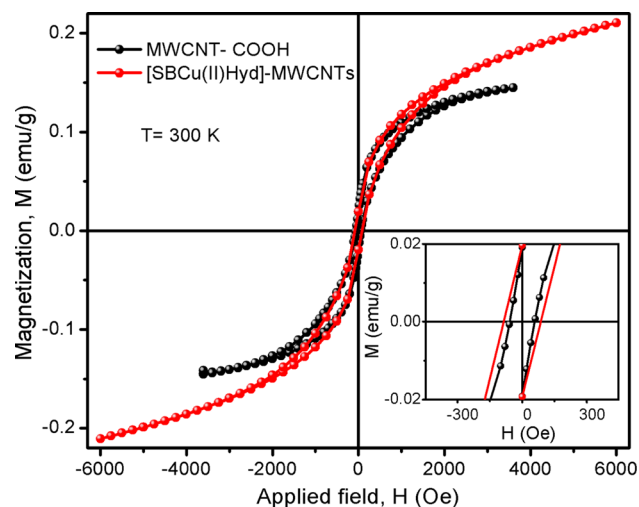


Figure 4 M versus H plots for MWCNT-COOH and [SBCu(II)Hyd]-MWCNTs. The inset shows enlarged view of hysteresis plot.

Table 3 Field-dependent magnetization data for MWCNT-COOH and [SBCu(II)Hyd]-MWCNTs at RT

Material	H_c (Oe)	M_r (emu/g)	M_s (emu/g)
MWCNT-COOH	59.94	0.0189	0.144
[SBCu(II)Hyd]-MWCNTs	88.43	0.0196	0.209

has been measured at 0.6 T (6000 Oe) in the temperature range 0–300 K (Fig. S8). The FC and ZFC curves overlapped in high temperature range (125–300 K) and splitting in FC and ZFC curves starts almost at around 125 K for both MWCNT-COOH and [SBCu(II)Hyd]-MWCNTs. The peak in FC and ZFC curves of MWCNT-COOH is signature of antiferromagnetic interaction with phase transition temperature (T_N) 62 K. For [SBCu(II)Hyd]-MWCNTs, the FC and ZFC curves show phase transitions at 62 and 51 K (T_N), respectively, suggesting antiferromagnetic interaction along with the ferromagnetic characteristic of material [63]. The χ^{-1} versus T plots for MWCNT-COOH and [SBCu(II)Hyd]-MWCNTs are displayed in Fig. 5. Fitting of linear portion of χ^{-1} versus T plot of both the materials with Curie-Weiss law, $\chi = C/(T - \theta)$, where χ is magnetic susceptibility, C is Curie constant, T is absolute temperature and θ is Weiss temperature [64] results negative θ value. This is, further, indication of antiferromagnetic interaction of domains in both MWCNT-COOH and [SBCu(II)Hyd]-MWCNTs. The value of θ is less negative for

[SBCu(II)Hyd]-MWCNTs (– 7.5 K) compared to that of MWCNT-COOH (– 60.8 K) and suggests weaker antiferromagnetic interactions in [SBCu(II)Hyd]-MWCNTs in comparison with that of MWCNT-COOH.

DC electrical conductivity study

The pellets of MWCNT-COOH and [SBCu(II)Hyd]-MWCNTs diameter (5 mm) and thicknesses (0.8 & 1.0 mm) were prepared using hand operated hydraulic press. The current versus voltage (I - V) characteristics (Fig. S9) were used to evaluate the bulk resistance of the materials. The direct current (DC) electrical conductivity of materials was evaluated with resistance and pellet thickness value by employing relation:

$$\sigma = \frac{1}{\rho} = \frac{L}{RA}$$

where ρ , L and A are electrical resistivity, thickness of the conductive pellet and cross-sectional area of the electrode, respectively. The value of electrical conductivity for MWCNT-COOH and [SBCu(II)Hyd]-MWCNTs was calculated to be 21.27 and 62.50 Sm^{-1} , respectively (Table 4). The electrical conductivity of [SBCu(II)Hyd]-MWCNTs was found to be larger than that of MWCNT-COOH due to extended conjugation and the presence of several Cu (II) metal ions on the surface of MWCNTs.

Electrochemical measurements

Electrochemical properties of GC/MWCNT-COOH and GC/[SBCu(II)Hyd]-MWCNTs electrodes were explored through CV and EIS experiments. Measurements were done using three electrodes one compartment system with a glassy carbon working electrode (area, 0.071 cm^2), a counter electrode (Pt wire) and a standard reference electrode (mercury/mercury oxide electrode) in 2.0 mM $\text{Fe}(\text{CN})_6^{3-/4-}$ (equimolar ratio) solution containing 0.1 M KCl. Both electrodes have well-defined redox characteristics (Fig. 6). The oxidative peak currents (I_{ox}) recorded for GC/MWCNT-COOH and GC/[SBCu(II)Hyd]-MWCNTs electrodes were found 22.4 and 25.5 μA , respectively. As compared to GC/MWCNT-COOH, the higher anodic current for GC/[SBCu(II)Hyd]-MWCNTs reveals its greater conductivity. The

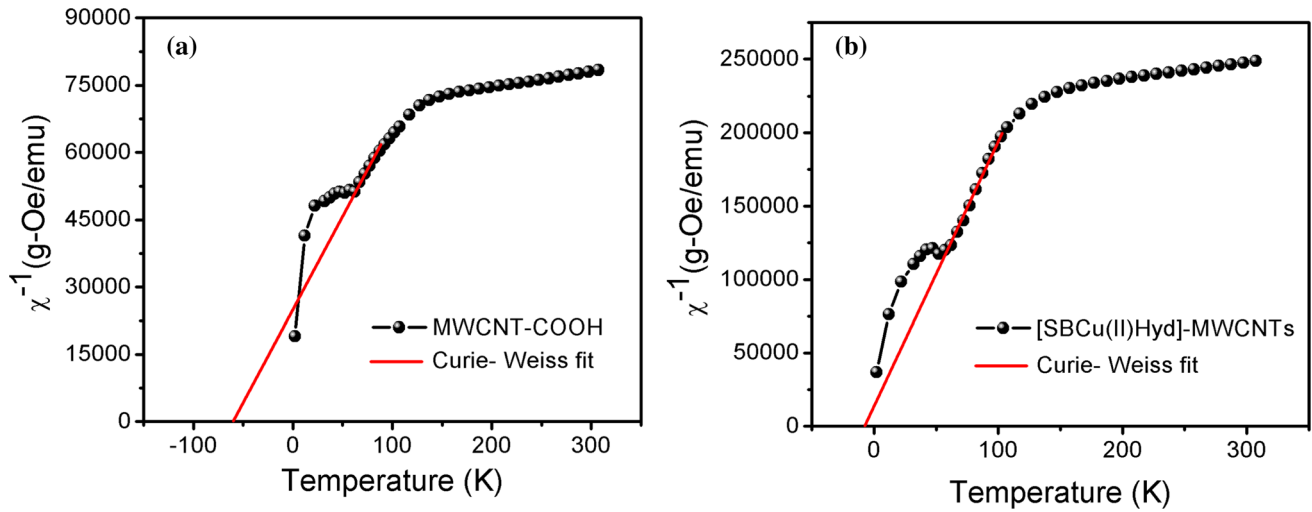


Figure 5 Inverse magnetic susceptibility with temperature plot for (a) MWCNT-COOH and (b) [SBCu(II)Hyd]-MWCNTs.

Table 4 Electrical resistance (*R*), specific resistance or resistivity (ρ) and conductivity (σ) for MWCNT-COOH and [SBCu(II)Hyd]-MWCNTs

Material	<i>R</i> (Ω)	ρ (Ω m)	σ (Sm^{-1})
MWCNT-COOH	2.25	0.047	21.27
[SBCu(II)Hyd]-MWCNTs	0.72	0.016	62.50

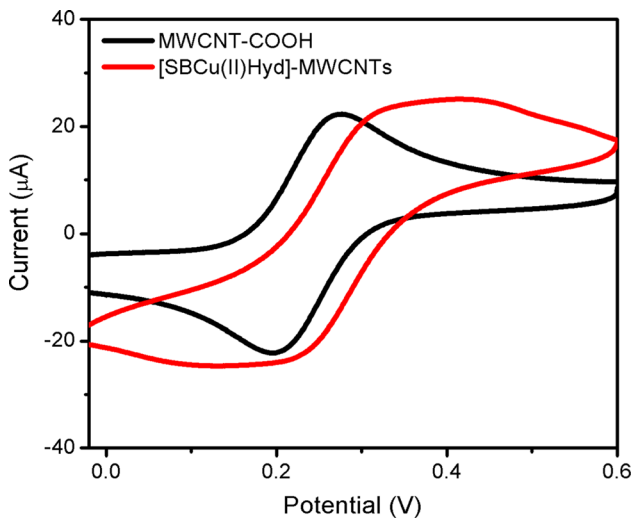


Figure 6 CV plots of GC/MWCNT-COOH and GC/[SBCu(II)Hyd]-MWCNTs electrodes in 2.0 mM $\text{Fe}(\text{CN})_6^{3-/4-}$ (1:1 molar ratio) solution in 0.1 M KCl.

electrochemically active surface area (ECSA) has been calculated using the Randles-Sevcik equation [65].

$$I_p = 2.99 \times 10^5 A C n (\nu D)^{1/2}$$
 where I_p , A , C , n , ν , and D are the peak current, electroactive surface area,

concentration of the reactive species (2.0 mM), number of electrons taking part in the reaction (here, $n = 1$), scan rate (0.02 V s^{-1}), and diffusion coefficient ($6.3 \times 10^{-6} \text{ cm}^2 \text{ s}^{-1}$) of the reactant species, respectively. The electroactive surface area of GC/MWCNT-COOH and GC/[SBCu(II)Hyd]-MWCNTs has been calculated to be 0.1 and 0.12 cm^2 , respectively.

GC/MWCNT-COOH and GC/[SBCu(II)Hyd]-MWCNTs electrodes were used to investigate electrical resistance and interfacial properties of materials using 0.1 M KCl solution containing 5.0 mM $\text{Fe}(\text{CN})_6^{3-/4-}$ in equimolar ratio (1:1), in 100 kHz to 0.1 Hz frequency region at 0.2 V by recording EIS spectra. Nyquist plots of GC/MWCNT-COOH and GC/[SBCu(II)Hyd]-MWCNTs electrodes (Fig. 7a, b) show depressed semicircle curves across a broad frequency spectrum, suggesting non-Debye type of relaxation in both materials [35, 40, 66]. These plots have been in ZsimpWin 3.21 simulating software as shown in Fig. 7c. This resulted in the best fit Randle’s equivalent circuit model, ($R_s Q(R_{ct} O)$); R_s (the solution resistance), R_{ct} (the charge transfer resistance), Q (an interfacial double layer capacitance here expressed by constant phase element) and O (the hyperbolic tangent impedance element) [41, 67].

Table 5 summarizes the values of these parameters in brief. The R_{ct} values observed for GC/MWCNT-COOH and GC/[SBCu(II)Hyd]-MWCNTs are found to be 4.23×10^2 and $7.7 \times 10^{-2} \Omega$, respectively. The lower R_{ct} value of GC/[SBCu(II)Hyd]-MWCNTs has verified their superior conductivity [68]. These

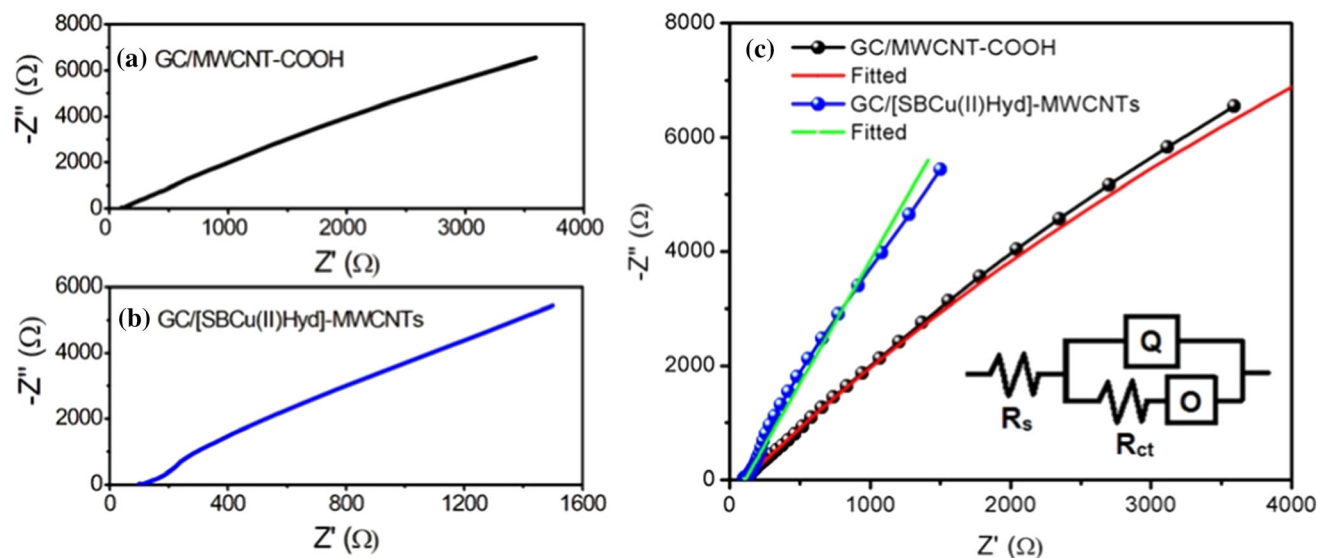


Figure 7 Nyquist plots for the electrodes (a) GC/MWCNT-COOH and (b) GC/[SBCu(II)Hyd]-MWCNTs in 2.0 mM $\text{Fe}(\text{CN})_6^{3-/4-}$ (1:1 molar ratio) solution in 0.1 M KCl obtained at a potential of 0.2 V and a frequency range of 100 kHz to 0.1 Hz.

(c) Fitted curves along with Nyquist plots and the most suitable Randle's equivalent circuit, ($R_s Q(R_{ct}O)$) corresponding to the Nyquist plots is shown in the inset.

Table 5 EIS parameters for GC/MWCNT-COOH and GC/[SBCu(II)Hyd]-MWCNTs electrodes

Parameter	GC/MWCNT-COOH	GC/[SBCu(II)Hyd]-MWCNTs
R_s (Ω)	112.8	109
Q- Y_0	1.1×10^{-4}	1.9×10^{-4}
Q-n	0.8	0.8
R_{ct} (Ω)	4.23×10^2	7.7×10^{-2}
O- Y_0	4.95×10^{-5}	1.33×10^{-19}
O-B	3.66	1.54×10^5

findings are in well agreement with the results of CV study.

For investigating capacitance and dielectric behavior of GC/MWCNT-COOH and GC/[SBCu(II)Hyd]-MWCNTs, the real (C') and imaginary part (C'') of cell capacitance were obtained from capacitance by using following equations:

$$C'(\omega) = \frac{-Z''(\omega)}{\{\omega|Z(\omega)|^2\}}$$

$$C''(\omega) = \frac{-Z'(\omega)}{\{\omega|Z(\omega)|^2\}}$$

where Z' , Z'' and Z are real, imaginary and total impedance of the cell, respectively, the angular frequency of the AC wave signal represented by ω is related to frequency (f , Hz) as $\omega = 2\pi f$, [41, 66, 69]. Frequency dependence of the cell capacitance for electrodes GC/MWCNT-COOH and GC/

[SBCu(II)Hyd]-MWCNTs is shown in Fig. S10. Initially, capacitance decreases sharply with increase of the frequency for both electrodes, however, around 350 Hz, it reaches saturation point (as shown in inset), as the charge carriers are unable to respond to the applied AC wave impulses at such high frequencies.

Further, GC/MWCNT-COOH and GC/[SBCu(II)Hyd]-MWCNTs electrodes were used to obtain the Mott-Schottky, M-S plots ($1/C_{sc}^2$ vs. V) (Fig. 8) [41] by recording the impedance in a solution of 0.1 M KCl containing 2.0 mM $\text{Fe}(\text{CN})_6^{3-}/\text{Fe}(\text{CN})_6^{4-}$ (1:1 molar ratio) with varying potential (V) at frequency 100 Hz. Flat band potentials (V_{fb}) of GC/MWCNT-COOH and GC/[SBCu(II)Hyd]-MWCNT were acquired by putting an intercept at the potential axis by extension of lines from the best suitable linear region of the M-S plot. The values are found to be -0.18 and -0.15 V, respectively (Table 6). The

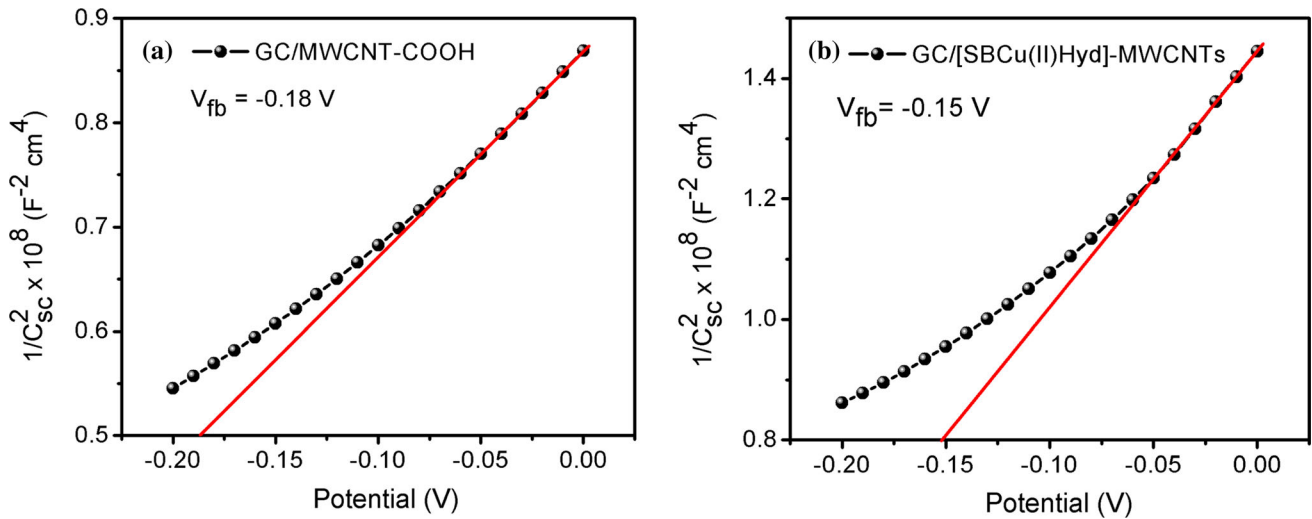


Figure 8 Capacitance of the GC/MWCNT-COOH and GC/[SBCu(II)Hyd]-MWCNTs electrodes as a function of potential (Mott-Schottky plots).

Table 6 Mott-Schottky electrochemical analysis parameters for GC/MWCNT-COOH and GC/[SBCu(II)Hyd]-MWCNTs

Material	Slope	V _{fb} (V)	ε
GC/MWCNT-COOH	4.0 × 10 ⁸	- 0.18	2.5 × 10 ¹¹ /N _D
GC/[SBCu(II)Hyd]-MWCNTs	19.86 × 10 ⁸	- 0.15	7.0 × 10 ¹⁰ /N _D

positive shift in V_{fb} of GC/[SBCu(II)Hyd]-MWCNTs in comparison with GC/MWCNT-COOH indicated better conductivity of metal complex modified MWCNTs. The slopes for GC/MWCNT-COOH and GC/[SBCu(II)Hyd]-MWCNTs were obtained from linear portion of plots and were found to be 4.0 × 10⁸ and 19.86 × 10⁸, respectively. The increased slope value for GC/[SBCu(II)Hyd]-MWCNTs is also suggesting its more conductive behavior. Positive slope values show n-type semiconducting nature of both materials [69]. Additionally, for a reference donor density (N_D) of the materials, the dielectric constants for GC/MWCNT-COOH and GC/[SBCu(II)Hyd]-MWCNTs electrodes were calculated by equating the slope with 1.41 × 10²⁰/ ε N_D [70]. Hence, as the donor density is related to conductivity as σ = enμ, where e is the electronic charge, n is carriers concentration, μ is mobility, and σ is the electrical conductivity of material [71], the maximum charge carriers concentration is expected for GC/[SBCu(II)Hyd]-MWCNTs electrode. This outcome is quite consistent with the findings of the DC conductivity, CV, and EIS studies.

Optical and electrochemical band gap studies

The Tauc’s plots (Fig. S11) were obtained from UV-visible spectra of MWCNT-COOH and [SBCu(II)Hyd]-MWCNTs in MeOH& DMF and in solid state (Nujol mull). The optical band gap (E_g^{opt}) is evaluated by using Tauc’s relation as given below,

$$(\alpha hv)^n = A(hv - E_g)$$

where α is the absorption coefficient in cm⁻¹, hv is the photon’s energy, and A is a constant and n is 2 & ½ for direct & indirect allowed transition, respectively [41, 72]. The direct allowed transitions, i.e., (αhv)² vs. hv plot was observed to have greater linearity than the indirect allowed transition plot ((αhv)^{1/2} vs. hv), and hence, the E_g^{opt} value was obtained by extrapolating the linear portion of (αhv)² versus hv plot to α → 0 [72]. In MeOH & DMF and solid state, the values of E_g^{opt} for MWCNT-COOH are found to be 3.23, 2.87 and 1.35 eV, respectively (Fig. S11 a, b & c) and for [SBCu(II)Hyd]-MWCNTs the values are 2.69, 2.47 and 1.18 eV, respectively (Fig. S11 d, e & f). The E_g^{opt} of materials is smaller in DMF compared to MeOH, which may be attributed to lower polarity and high Lewis basicity of DMF [47]. Whereas, the

E_g^{opt} values for MWCNT-COOH and [SBCu(II)Hyd]-MWCNTs decreased more in the solid state due to increased molecule association and aggregation [48]. The E_g^{opt} of [SBCu(II)Hyd]-MWCNTs is observed to be smaller to that of MWCNT-COOH in both solvents and solid state, that signified improved conductivity of [SBCu(II)Hyd]-MWCNTs after chemical modification.

By estimating frontier orbitals (HOMO and LUMO) using non-aqueous CV, the electrochemical band gap (E_g^{CV}) (Fig. S12) of materials was determined. A materials drop coated GC working electrode, Ag/AgCl (non-aqueous) reference electrode and counter electrode Pt wire were used to obtain the CV curves of GC/MWCNT-COOH and GC/[SBCu(II)Hyd]-MWCNTs at a scan rate of 10 mVs^{-1} with the potential range of -0.6 to 1.4 V . A solution (0.1 M) of tetrabutylammonium perchlorate (TBAP) in anhydrous acetonitrile was used as the supporting electrolyte and ferrocene couple (for an absolute energy level relative to vacuum of 4.80 eV) served as an internal reference. The anodic and cathodic peak potentials for Fc/Fc⁺ redox couple were found to be 0.579 and 0.515 V , respectively (Fig. S12a), giving half-wave potential of the ferrocene/ferrocenium ($E_{1/2, \text{Fc/Fc}^+}$) as 0.547 V calculated by using relation:

$$E_{1/2\text{Fc/Fc}^+} = (E_{\text{anodic peak potential}} + E_{\text{cathodic peak potential}})/2$$

The HOMO and LUMO levels were calculated from redox onset potential of CV plot (Fig. S12b) by using equations:

$$E_{\text{HOMO}} = -\left(E_{\text{ox}}^{\text{onset}} - E_{1/2\text{Fc/Fc}^+}\right) - 4.80 \text{ eV}$$

$$E_{\text{LUMO}} = -\left(E_{\text{red}}^{\text{onset}} - E_{1/2\text{Fc/Fc}^+}\right) - 4.80 \text{ eV}$$

Subsequently, electrochemical band gap (E_g^{CV}) has been calculated by using relation [72], Electrochemical band gap, (E_g^{CV}) = $(E_{\text{LUMO}} - E_{\text{HOMO}})\text{eV}$

The values of E_g^{CV} are found to be 1.392 and 1.242 eV for GC/MWCNT-COOH and GC/

[SBCu(II)Hyd]-MWCNTs electrodes, respectively (Table 7). The lower value of E_g^{CV} for GC/[SBCu(II)Hyd]-MWCNTs electrode compared to that of GC/MWCNT-COOH suggested its better conducting property.

Electrochemical sensing of glucose

Cyclic voltammetry is considered as the reliable and simplest analytical technique to obtain qualitative and quantitative information of any electroactive species [73]. This technique is beneficial for the study of electrochemical behavior of the analytes being determined [74]. Therefore, CV analysis was employed to examine the electrochemical behavior of glucose at the modified GC as working electrode in 0.1 M KOH solution in the potential ranging from 0.0 to 0.6 V with scan rate of 20 mVs^{-1} . Figure 9 shows cyclic voltammograms of the MWCNT-COOH and [SBCu(II)Hyd]-MWCNTs on the GC electrodes with and without 1.0 mM glucose. The oxidation of glucose at GC/[SBCu(II)Hyd]-MWCNTs electrode shows a very high current ($104 \mu\text{A}$) as compared to GC/MWCNT-COOH electrode. The oxidation current obtained at GC/MWCNT-COOH electrode is not significant. The oxidation potential obtained for glucose at GC/[SBCu(II)Hyd]-MWCNTs was found to be 0.42 V .

The effect of glucose concentration on the current response was monitored by the amperometry technique. Amperometric determination of glucose has been done by applying a potential of 0.4 V at the GC/[SBCu(II)Hyd]-MWCNTs electrode in 0.1 M KOH solution. The current response has been recorded with the gradual addition of glucose $1.0 \mu\text{M}$ to 5.0 mM at the interval of 50 s (Fig. 10). This shows increase in current of glucose ($1.0 \mu\text{M}$ to 5.0 mM) in 0.1 M KOH solution at potential of 0.4 V . The calibration plot for the glucose determination is shown in the inset. The error bars of the calibration plot are based on the standard deviation of the three measurements.

Table 7 Optical and electrochemical band gaps for MWCNT-COOH and GC/[SBCu(II)Hyd]-MWCNTs

Material	$E_g^{\text{opt}} / \text{EtOH}$ (eV)	$E_g^{\text{opt}} / \text{DMF}$ (eV)	$E_g^{\text{opt}} / \text{solid state}$ (eV)	E_g^{CV} (eV)
MWCNT-COOH	3.23	2.87	1.35	0.93
[SBCu(II)Hyd]-MWCNTs	2.69	2.47	1.18	0.52

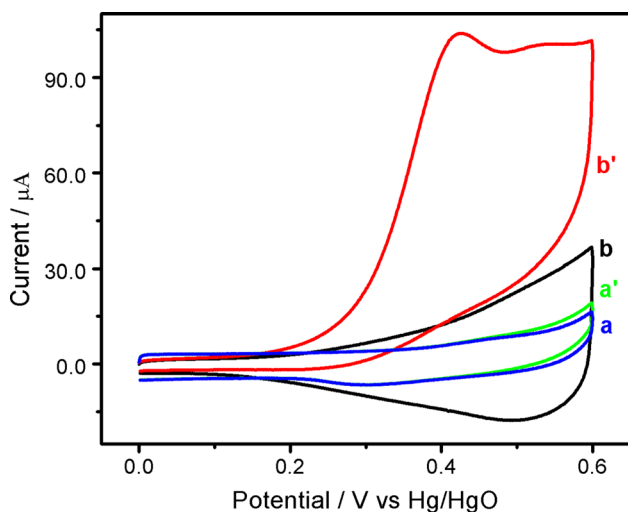


Figure 9 CV responses for GC/MWCNT-COOH (a & a') and GC/[SBCu(II)Hyd]-MWCNTs (b & b') in 0.1 M KOH solution without (a & b) and with (a' & b') of 1.0 mM glucose.

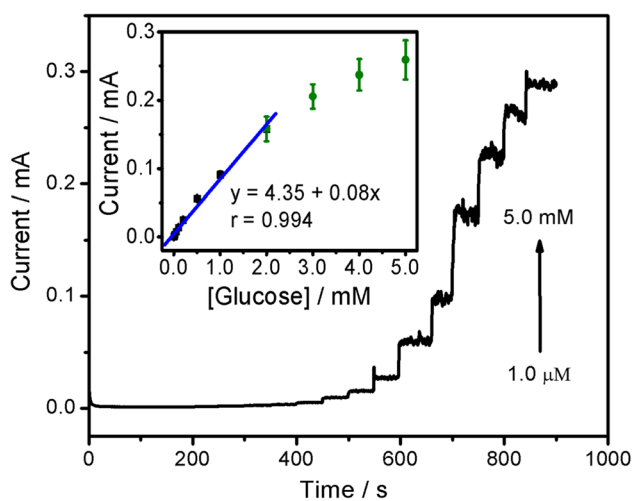


Figure 10 Amperometric response at GC/[SBCu(II)Hyd]-MWCNTs for different concentrations.

The plot of current versus concentration was obtained using the amperometric data and is shown in the inset of Fig. 10. The range of glucose was varying from 1.0 μM to 5.0 mM and a linear calibration plot from 1.0 μM to 2.0 mM is observed. However, at higher concentration (2.0–5.0 mM), the calibration plot deviates from the linearity. This deviation at the high concentration of glucose may be due to the plausible accumulation of the oxidation product on the surface of the electrode, which may saturate the active site, thus decreasing the diffusion of glucose [75, 76].

The sensitivity of the prepared sensor has been evaluated from the slope of the calibration plot and the geometrical area of the electrode and is found to be $1.1 \mu\text{A}\mu\text{M}^{-1} \text{cm}^{-2}$. The limit of detection (LOD) was determined by relation:

$$\text{LOD} = 3\sigma/m$$

where σ is the standard deviation of blank and m is the slope of the calibration plot [77]. The LOD is found to be 0.09 μM . The sensor represents high sensitivity and low LOD. The modified electrode, according to its linear range, can detect glucose in the range of 1.0 μM to 2.0 mM. The healthy individual has 5–7 mM of glucose while the diabetic individual may have a glucose level of up to 30 mM [78, 79]. This indicates that with a proper dilution of the sample, these electrodes can be used to measure the glucose levels in both healthy and diabetic people.

To get insight into the selectivity of the modified electrode, an interference study has been performed and is shown in Fig. S13. Amperometry technique was used (at an applied potential of 0.4 V) to study the selectivity at GC/[SBCu(II)Hyd]-MWCNTs electrode and possible interfering species (urea, cysteine, uric acid, acetaminophen, acetylsalicylic acid, NaCl, Mg^{2+} , and Ca^{2+}) were introduced into the electrolyte (0.1 M KOH) at regular intervals of 50 s in 0.1 mM concentrations and shown in Fig. S13a. In the presence of interfering species, the current response for glucose oxidation shows negligible changes except for acetaminophen, where a slight increase in the current response (14.5%) is observed. This clearly shows that the synthesized sensor is highly selective for glucose oxidation. The reproducibility study has been performed at GC/[SBCu(II)Hyd]-MWCNTs electrode by recording ten CV responses at the intervals of one minute in the presence of 1.0 mM glucose in 0.1 M KOH. The monitored responses are shown as a bar diagram in Fig. S13b in the form of relative current value. The response was maintained up to 91.2% after ten measurements, this confirms the reproducibility of the proposed electrode. A stability study is also performed at GC/[SBCu(II)Hyd]-MWCNTs electrode by amperometry technique (applied potential 0.4 V). The amperometry response is recorded till 1700s, and however, 1.0 mM of glucose is added into the electrolyte (0.1 M KOH) at the 200th s and the current response is monitored up to 1700s as depicted in Fig. S13c. Negligible decrease (1.16%)

is observed which shows the stable nature of the electrochemical sensor.

Conclusions

A new bifunctional nanomaterial, copper (II) Schiff-base complex functionalized MWCNTs, [SBCu(II)-Hyd]-MWCNTs with greater electrical conductivity and magnetic characteristics was synthesized by chemical treatment of carboxylated MWCNTs. FT-IR, UV-Vis, Raman, TGA, XPS, PXRD, TEM, EDAX and elemental mapping studies revealed the chemical modification of MWCNT-COOH. Powder XRD and TEM analyses indicated no alteration in crystal structure and tubular framework of MWCNT-COOH after modification. The room temperature field-dependent magnetization revealed typical ferromagnetic properties with enhanced coercivity saturation and remanent magnetization of [SBCu(II)Hyd]-MWCNTs compared to that of MWCNT-COOH. The temperature-dependent magnetization revealed antiferromagnetic exchange interaction along with the ferromagnetic characteristics for both MWCNT-COOH and [SBCu(II)Hyd]-MWCNTs. This is also confirmed from temperature-dependent inverse magnetic susceptibility (χ^{-1} vs. T) plots. The less negative θ value obtained from χ^{-1} versus T plot for [SBCu(II)Hyd]-MWCNTs than that of MWCNT-COOH is also an indication for less antiferromagnetic interaction in [SBCu(II)Hyd]-MWCNTs. Further, MWCNT-COOH with lower electrical conductivity was modified into better conducting material [SBCu(II)Hyd]-MWCNTs with increased DC electrical conductivity, higher oxidation current, lower charge transfer resistance, and lower optical & electrochemical band gaps. Both MWCNT-COOH and [SBCu(II)Hyd]-MWCNTs exhibited n-type semiconducting behavior. The positive shifting in the flat band potential (V_{fb}) of [SBCu(II)Hyd]-MWCNTs to that of MWCNT-COOH also signified enhanced electric conductive property of the material, [SBCu(II)Hyd]-MWCNTs. Subsequently, the modified material, [SBCu(II)Hyd]-MWCNTs, was utilized as electrochemical sensor for the determination of glucose. The value of sensitivity and limit of detection (LOD) for GC/[SBCu(II)Hyd]-MWCNTs electrode was found to be $1.1 \mu\text{A } \mu\text{M}^{-1} \text{cm}^{-2}$ and $0.09 \mu\text{M}$, respectively.

Acknowledgements

I would like to delightedly acknowledge Department of Science and Technology (DST Scheme No. SR/NM/NS-1212/2013), New Delhi, India, for giving me a research fellowship, which served as financial support, as well as the VSM facilities to do my research. Incentive fund from IOE, B. H. U, (IOE/Dev. Scheme No. 6031), Ministry of Human Resource and Development is also acknowledged. I am also thankful to Late Prof. O. N. Srivastava, Department of Physics for providing TEM facility. Central Instrumentation Facility of I.I.T. B.H.U is acknowledged for temperature dependent magnetization studies. Advanced Centre for Material Sciences, IIT Kanpur is highly acknowledged for XPS analysis of synthesized materials.

Author's contribution

RG took part in conceptualization, experimental setup, and preparation of materials, formal analysis, investigation and writing original draft. Formal analysis, investigation and writing—review & editing were performed by MY. The selectivity, reproducibility and stability studies to verify the performance of proposed glucose sensor have been investigated by SS. The electrochemical studies were supervised by VG. Validation, investigation, resources, writing- review & editing, supervision and project administration were achieved by BS.

Data availability

The raw/processed data required to reproduce these findings cannot be shared at this time due to legal or ethical reasons.

Declarations

Conflict of interest The Authors have no conflicts of interest to declare.

Supplementary Information: The online version contains supplementary material available at <http://doi.org/10.1007/s10853-023-08774-z>.

References

- [1] Dwivedi N, Kumar S, Carey JD, Dhand C (2015) Functional nanomaterials for electronics, optoelectronics, and bioelectronics. *J Nanomater* 2015:1–1
- [2] Wongkaew N, Simsek M, Griesche C, Baeumner AJ (2018) Functional nanomaterials and nanostructures enhancing electrochemical biosensors and lab-on-a-chip performances: recent progress, applications, and future perspective. *Chem Rev* 119(1):120–194
- [3] Xue X, Wang F, Liu X (2011) Emerging functional nanomaterials for therapeutics. *J Mater Chem* 21(35):13107–13127
- [4] Zhu C, Liu T, Qian F, Chen W, Chandrasekaran S, Yao B, Song Y, Duoss EB, Kuntz JD, Spadaccini CM, Worsley MA (2017) 3D printed functional nanomaterials for electrochemical energy storage. *Nano Today* 15:107–120
- [5] Zaera F (2013) Nanostructured materials for applications in heterogeneous catalysis. *Chem Soc Rev* 42(7):2746–2762
- [6] Yin Y, Talpin D (2013) The chemistry of functional nanomaterials. *Chem Soc Rev* 42(7):2484–2487
- [7] Ghomi LS, Behzad M, Tarahhomi A, Arab A (2017) Crystal structures, DFT calculations, and Hirshfeld surface analyses of two new copper (II) and nickel (II) Schiff base complexes derived from meso-1, 2-diphenyl-1, 2-ethylenediamine. *J Mol Struct* 1150:214–226
- [8] Canali L, Sherrington DC (1999) Utilisation of homogeneous and supported chiral metal (salen) complexes in asymmetric catalysis. *Chem Soc Rev* 28(2):85–93
- [9] Jones RD, Summerville DA, Basolo F (1979) Synthetic oxygen carriers related to biological systems. *Chem Rev* 79(2):139–179
- [10] Casas JS, Couce MD, Sordo J (2012) Coordination chemistry of vitamin B6 and derivatives: a structural overview. *Coord Chem Rev* 256(23–24):3036–3062
- [11] Oiye ÉN, Ribeiro MF, Katayama JM, Tadini MC, Albino MA, Eleotério IC, Magalhães J, Castro AS, Silva RS, da Júnior CJW, Dockal ER (2019) Electrochemical sensors containing Schiff bases and their transition metal complexes to detect analytes of forensic, pharmaceutical and environmental interest. A review. *Crit Rev Anal Chem* 49(6):488–509
- [12] More MS, Joshi PG, Mishra YK, Khanna PK (2019) Metal complexes driven from Schiff bases and semicarbazones for biomedical and allied applications: a review. *Mat Today Chem* 14:100195
- [13] Gebreyesus ST, Khan MA (2015) An overview on metal complexes of selected schiff-bases with their electrochemical and sensor aspects. *J Chem Chem Sci* 5(1):19–27
- [14] Garoufis A, Hadjikakou SK, Hadjiliadis NJ (2009) Palladium coordination compounds as anti-viral, anti-fungal, anti-microbial and anti-tumor agents. *Coord Chem Rev* 253(9–10):1384–1397
- [15] Jeevadason AW, Murugavel KK, Neelakantan MA (2014) Review on Schiff bases and their metal complexes as organic photovoltaic materials. *Renew Sustain Energy Rev* 36:220–227
- [16] Zhang J, Xu L, Wong WY (2018) Energy materials based on metal Schiff base complexes. *Coord Chem Rev* 355:180–198
- [17] Miyasaka H, Saitoh A, Abe S (2007) Magnetic assemblies based on Mn (III) salen analogues. *Coord Chem Rev* 251(21–24):2622–2664
- [18] Kumar KS, Bayeh Y, Gebretsadik T, Elemo F, Gebrezgiabher M, Thomas M, Ruben M (2019) Spin-crossover in iron (II)-Schiff base complexes. *Dalton Trans* 48(41):15321–15337
- [19] Wang L, Jiao S, Zhang W, Liu Y, Yu G (2013) Synthesis, structure, optoelectronic properties of novel zinc Schiff-base complexes. *Chi Sci Bull* 58:2733–2740
- [20] Al-Hazmi GA, El-Metwally N (2017) A series of nickel (II) complexes derived from hydrazide derivatives, electrochemical, thermal and spectral studies. *Arab J Chem* 10:S1003–S1013
- [21] Borthakur R, Kumar A, De AK, Lal RA (2019) Synthesis, characterization and electrochemical properties of copper (II) complexes derived from succinoyldihydrazine Schiff base ligands. *Arab J Chem* 12(8):2192–2205
- [22] Dhanakodi P, Jayandran M, Balasubramanian V (2018) Syntheses and characterization of complexes of copper (II) with Schiff-base ligands derived from 2, 6-diacetylpyridine: spectroscopic, thermal behavior, magnetic moment and photoluminescent studies. *J Mater Sci Mater Electron* 29:7526–7530
- [23] Guo Y, Hu X, Zhang X, Pu X, Wang Y (2019) The synthesis of a Cu (ii) Schiff base complex using a bidentate N₂O₂ donor ligand: crystal structure, photophysical properties, and antibacterial activities. *RSC Adv* 9(71):41737–41744
- [24] Sridara T, Upan J, Saianand G, Tuantranont A, Karuwan C, Jakmunee J (2020) Non-enzymatic amperometric glucose sensor based on carbon nanodots and copper oxide nanocomposites electrode. *Sensors* 20(3):808
- [25] Kannan P, Maiyalagan T, Marsili E, Ghosh S, Guo L, Huang Y, Rather JA, Thirupathi D, Niedziolka-Jönsson J, Jönsson-Niedziolka M (2017) Highly active 3-dimensional cobalt oxide nanostructures on the flexible carbon substrates for enzymeless glucose sensing. *Analyst* 142(22):4299–4307
- [26] Haghparas Z, Kordrostami Z, Sorouri M, Rajabzadeh M, Khalifeh R (2020) Fabrication of non-enzymatic

- electrochemical glucose sensor based on nano-copper oxide micro hollow-spheres. *Biotechnol Bioprocess Eng* 25:528–535
- [27] Jiang D, Liu Q, Wang K, Qian J, Dong X, Yang Z, Du X, Qiu B (2014) Enhanced non-enzymatic glucose sensing based on copper nanoparticles decorated nitrogen-doped graphene. *Biosens Bioelectron* 54:273–278
- [28] Baingane A, Narayanan JS, Slaughter G (2018) Sensitive electrochemical detection of glucose via a hybrid self-powered biosensing system. *Sens Bio-sens Res* 20:41–46
- [29] Dai Z, Yang A, Bao X, Yang R (2019) Facile non-enzymatic electrochemical sensing for glucose based on Cu₂O–BSA nanoparticles modified GCE. *Sensors* 19(12):2824
- [30] Perušković DS, Stevanović NR, Kovačević GN, Stanković DM, Lolić AĐ, Baošić RM (2020) Application of N, N'-Bis (acetylacetonato) propylenediimine copper (II) complex as mediator for glucose biosensor. *Chem Sel* 5(5):1671–1675
- [31] Batchelor-McAuley C, Wildgoose GG, Compton RG, Shao L, Green ML (2008) Copper oxide nanoparticle impurities are responsible for the electroanalytical detection of glucose seen using multiwalled carbon nanotubes. *Sens Act B Chem* 132(1):356–360
- [32] Hu C, Hu S (2009) Carbon nanotube-based electrochemical sensors: principles and applications in biomedical systems. *J Sens*. <https://doi.org/10.1155/2009/187615>
- [33] Sonkar PK, Ganesan V, John SA, Yadav DK, Gupta R (2016) Non-enzymatic electrochemical sensing platform based on metal complex immobilized carbon nanotubes for glucose determination. *RSC Adv* 6(108):107094–107103
- [34] Rezaeinasab M, Benvidi A, Tezerjani MD, Jahanbani S, Kianfar AH, Sedighipoor M (2017) An electrochemical sensor based on Ni (II) complex and multi wall carbon nanotubes platform for determination of glucose in real samples. *Electroanalysis* 29(2):423–432
- [35] Hasanzadeh M, Hasanzadeh Z, Alizadeh S, Sayadi M, Nezhad NM, Sabzi E, R., & Ahmadi, S. (2020) Copper-nickel oxide nanofilm modified electrode for non-enzymatic determination of glucose. *J Electrochem Sci Eng* 10(3):245–255
- [36] Yang Z, Feng J, Qiao J, Yan Y, Yu Q, Sun K (2012) Copper oxide nanoleaves decorated multi-walled carbon nanotube as platform for glucose sensing. *Anal Methods* 4(7):1924–1926
- [37] Figiela M, Wysokowski M, Galinski M, Jesionowski T, Stepniak I (2018) Synthesis and characterization of novel copper oxide-chitosan nanocomposites for non-enzymatic glucose sensing. *Sens Act B Chem* 272:296–307
- [38] Bernasconi R, Mangogna A, Magagnin L (2018) Low cost inkjet fabrication of glucose electrochemical sensors based on copper oxide. *J Electrochem Soc* 65(8):B3176
- [39] Maaoui H, Teodoresu F, Wang Q, Pan GH, Addad A, Chtourou R, Szunerits S, Boukherroub R (2016) Non-enzymatic glucose sensing using carbon quantum dots decorated with copper oxide nanoparticles. *Sensors* 16(10):1720
- [40] Gupta R, Singh B (2020) Chemical modification of carboxylated MWCNTs for enhanced electrical conducting and magnetic properties. *Mat Sci Eng B* 262:114730
- [41] Bazarganipour M, Salavati-Niasari M (2016) Synthesis, characterization and chemical binding of a Ni (II) Schiff base complex on functionalized MWNTs; Catalytic oxidation of cyclohexene with molecular oxygen. *Chem Eng J* 286:259–265
- [42] Veisi H, Azadbakht R, Saeidifar F, Abdi MR (2017) Schiff base-functionalized multi walled carbon nanotubes to immobilization of palladium nanoparticles as heterogeneous and recyclable nanocatalyst for Suzuki reaction in aqueous media under mild conditions. *Catal Lett* 147:976–986
- [43] Singh MS, Tawade K (2000) Synthesis and characterization of some new organotin (IV) complexes of a Schiff base derived from salicylaldehyde and hydrazine hydrate. *Synth React Inorg Mat Org Chem* 30(6):1015–1022
- [44] Dikio CW, Ejidike IP, Mtunzi FM, Klink MJ, Dikio ED (2017) Hydrazide Schiff bases of acetylacetonate metal complexes: synthesis, spectroscopic and biological studies. *Int J Pharm Pharm Sci* 12:257–267
- [45] Lekshmy RK, Thara GS (2014) Synthesis and characterization of copper complexes of Schiff base derived from isatin and salicylic hydrazide. In: *AIP Conference Proceedings, American Institute of Physics* 1620(1): 230-234
- [46] Kolcu F, Kaya İ (2017) Synthesis, characterization and photovoltaic studies of oligo (acriflavine) via chemical oxidative polymerization. *RSC Adv* 7(15):8973–8984
- [47] Gupta M, Pal SK (2016) Triphenylene-based room-temperature discotic liquid crystals: a new class of blue-light-emitting materials with long-range columnar self-assembly. *Langmuir* 32(4):1120–1126
- [48] Zhang G, Yang D, Sacher E (2007) X-ray photoelectron spectroscopic analysis of Pt nanoparticles on highly oriented pyrolytic graphite, using symmetric component line shapes. *J Phy Chem C* 111(2):565–570
- [49] Ourari A, Derafa W, Aggoun D (2015) A novel copper (II) complex with an unsymmetrical tridentate-Schiff base: synthesis, crystal structure, electrochemical, morphological and electrocatalytic behaviors toward electroreduction of alkyl and aryl halides. *RSC Adv* 5(101):82894–82905
- [50] Reddy GR, Balasubramanian S, Chennakesavulu K (2014) Zeolite encapsulated Ni (ii) and Cu (ii) complexes with tetradentate N₂O₂ Schiff base ligand: catalytic activity towards oxidation of benzhydrol and degradation of rhodamine-B. *J Mater Chem A* 2(37):15598–15610

- [51] Bora SJ, Chetia B (2019) Synthesis of ynones at room temperature catalyzed by copper chloride cryptand complex under solvent free conditions. *Heliyon* 5(7):e02000
- [52] Gayen FR, Ali AA, Bora D, Roy S, Saha S, Saikia L, Goswamee RL, Saha B (2020) A ferrocene functionalized Schiff base containing Cu (II) complex: synthesis, characterization and parts-per-million level catalysis for azide alkyne cycloaddition. *Dalton Trans* 49(20):6578–6586
- [53] Vafakish B, Wilson LD (2020) Cu (II) Ion adsorption by Aniline grafted Chitosan and its responsive fluorescence properties. *Molecules* 25(5):1052
- [54] Bokobza LA, Zhang J (2012) Raman spectroscopic characterization of multiwall carbon nanotubes and of composites. *Express Polym Lett* 6(7):601
- [55] Park OK, Lee S, Joh HI, Kim JK, Kang PH, Lee JH, Ku BC (2012) Effect of functional groups of carbon nanotubes on the cyclization mechanism of polyacrylonitrile (PAN). *Polymer* 53(11):2168–2174
- [56] Salavati-Niasari M, Davar F, Bazarganipour M (2010) Synthesis, characterization and catalytic oxidation of paraxylene by a manganese (III) Schiff base complex on functionalized multi-wall carbon nanotubes (MWNTs). *Dalton Trans* 39(31):7330–7337
- [57] Wang F, Arai S, Endo M (2004) Metallization of multi-walled carbon nanotubes with copper by an electroless deposition process. *Electrochem Commun* 6(10):1042
- [58] Theivasanthi T, Alagar M (2010) X-ray diffraction studies of copper nanopowder. *arXiv preprint arXiv:1003.6068* Mar 3–1. <https://doi.org/10.48550/arXiv.1003.6068>
- [59] Zhao J, Xie Y, Guan D, Hua H, Zhong R, Qin Y, Fang J, Liu H, Chen J (2015) BaFe₂O₉-chitosan Schiff-base Ag (I) complexes embedded in carbon nanotube networks for high-performance electromagnetic materials. *Sci Rep* 5(1):1–1
- [60] Abdalla AM, Sahu RP, Wallar CJ, Chen R, Zhitomirsky I, Puri IK (2017) Nickel oxide nanotube synthesis using multi-walled carbon nanotubes as sacrificial templates for supercapacitor application. *Nanotechnology* 28(7):075603
- [61] Morales I, Costo R, Mille N, Da Silva GB, Carrey J, Hernandez A, De la Presa P (2018) High frequency hysteresis losses on γ -Fe₂O₃ and Fe₃O₄: Susceptibility as a magnetic stamp for chain formation. *Nanomaterials* 8(12):970
- [62] Akhtar AJ, Gupta A, Chakravorty D, Saha SK (2013) Antiferroquadrupolar ordering in Fe intercalated few layers graphene. *AIP Adv* 3(7):072124
- [63] Petrovský E, Kapička A (2006) On determination of the Curie point from thermomagnetic curves. *J Geophys Res Solid Earth*. <https://doi.org/10.1029/2006JB004507>
- [64] Gupta R, Singh B (2019) Enhancement of electrical conductivity and magnetic properties of bimetallic Schiff base complex on grafting to MWCNTs. *J Mater Sci Mater Electron* 30:11888–11906
- [65] Jahan M, Bao Q, Loh KP (2012) Electrocatalytically active graphene–porphyrin MOF composite for oxygen reduction reaction. *J Am Chem Soc* 134:6707–6713
- [66] Parida K, Dehury SK, Choudhary RN (2016) Structural, electrical and magneto-electric characteristics of BiMgFe-CeO₆ ceramics. *Phys Lett A* 380(48):4083–4091
- [67] Nan M, Bi Y, Xue H, Xue S, Long H, Pu L, Fu G (2019) Rapid determination of ochratoxin A in grape and its commodities based on a label-free impedimetric aptasensor constructed by layer-by-layer self-assembly. *Toxins* 11(2):71
- [68] Ali GA, Yusoff MM, Shaaban ER, Chong KF (2017) High performance MnO₂ nanoflower supercapacitor electrode by electrochemical recycling of spent batteries. *Ceram Inter* 43(11):8440–8448
- [69] Datta J, Das M, Dey A, Halder S, Ray SS (2017) Network analysis of semiconducting Zn_{1-x}Cd_xS based photosensitive device using impedance spectroscopy and current-voltage measurement. *Appl Surf Sci* 420:566–578
- [70] Villora EG, Shimamura K, Yoshikawa Y, Ujiie T, Aoki K (2008) Electrical conductivity and carrier concentration control in β -Ga₂O₃ by Si doping. *Appl Phys Lett* 92(20):202120
- [71] Rashad MM, Hassan AM, Nassar AM, Ibrahim NM, Mourtada A (2014) A new nano-structured Ni (II) Schiff base complex: synthesis, characterization, optical band gaps, and biological activity. *Appl Phys A* 117:877–890
- [72] Yunus K, Mutlu H, Gazi İ (2010) Uv-vis spectra and fluorescence properties of two iminoxime ligands and their metal complexes: optical band gaps. *Gazi Univ J Sci* 23(1):13–18
- [73] Guy OJ, Walker KAD (2016) Graphene functionalization for biosensor applications. *Biotechnol* 2016:85–141
- [74] Deroco PB, de FátimaGiarolaJ JDW, Lorga GA, Kubota LT (2020) Paper based electrochemical sensing devices. *Compr Anal Chem* 89:91–137
- [75] Gupta R, Rastogi PK, Ganesan V, Yadav DK, Sonkar PK (2017) Gold nanoparticles decorated mesoporous silica microspheres: a proficient electrochemical sensing scaffold for hydrazine and nitrobenzene. *Sens Act B Chem* 239:970–978
- [76] Zhang Y, Bo X, Nsabimana A, Han C, Li M, Guo L (2015) Electrocatalytically active cobalt-based metal–organic framework with incorporated macroporous carbon composite for electrochemical applications. *J Mater Chem A* 3(2):732–738
- [77] Yadav M, Ganesan V, Maiti B, Gupta R, Sonkar PK, Yadav DK, Walcarius A (2019) Sensitive determination of acetaminophen in the presence of dopamine and pyridoxine

facilitated by their extent of interaction with single-walled carbon nanotubes. *Electroanalysis* 31(12):2472–2479

- [78] Bruen D, Delaney C, Florea L, Diamond D (2017) Glucose sensing for diabetes monitoring: recent developments. *Sensors* 17:1866
- [79] Macaya DJ, Nikolou M, Takamatsu S, Mabeck JT, Owens RM, Malliaras GG (2007) Simple glucose sensors with micromolar sensitivity based on organic electrochemical transistors. *Sens Act B Chem* 123(1):374–378

Publisher's Note Springer Nature remains neutral with regard to jurisdictional claims in published maps and institutional affiliations.

Springer Nature or its licensor (e.g. a society or other partner) holds exclusive rights to this article under a publishing agreement with the author(s) or other rightsholder(s); author self-archiving of the accepted manuscript version of this article is solely governed by the terms of such publishing agreement and applicable law.